3-1-2007

Precision in Imaging Multivariate Optical Computing

Michael N. Simcock
University of South Carolina - Columbia

Michael L. Myrick
University of South Carolina - Columbia, myrick@sc.edu

Publication Info

Published in *Applied Optics*, Volume 46, Issue 7, 2007, pages 1066-1080.

Precision in imaging multivariate optical computing

Michael N. Simcock and Michael L. Myrick

Multivariate optical computing (MOC) is a method of performing chemical analysis using a multilayer thin-film structure known as a multivariate optical element (MOE). Recently we have been advancing MOC for imaging problems by using an imaging MOE (IMOE) in a normal-incidence geometry and employing normalization by the 1-norm. There are several important differences between the previously described 45° and the normal-incidence imaging, one of which is the measurement precision due to photon counting. We compare this precision to 45° MOC. We also discuss how MOE models with similar values of standard errors of calibration and prediction and similar gain values may vary in precision because of the sign or offset of the regression vector encoded in the IMOE spectrum. Experimental verification of a key result is provided by near-infrared imaging of slides coated with a dye-doped polymer film.

OCIS codes: 000.1570, 120.4570, 120.4610, 120.5630, 120.6200, 200.4560.

1. Introduction

Multivariate optical computing (MOC) is a method for quantifying the presence of a target spectral signature in the presence of other interfering spectral signatures.[1,2] In chemistry this is typically done to determine the quantity of a given compound within a mixture of other interfering compounds, where the analyte and interferents have overlapping optical spectra in the spectral region used for the quantification.

The traditional method for isolating and measuring a target spectral signature among interfering species is to acquire a series of calibration spectra with known analyte concentrations from a reference method and then to subject them to multivariate calibration. Methods such as principal components regression and partial least squares are used to identify a spectral pattern that overlaps the analyte spectrum while being orthogonal or nearly orthogonal to the spectra of interfering species.[3,4] This overlapping pattern is commonly known as a regression vector. Using the language of linear algebra, the regression vector ($\mathbf{b}$) is then used to give an estimate, $\hat{y}_i$, of the analyte concentration in an unknown sample $\mathbf{i}$ by recording the spectrum, $\mathbf{x_i}$, of the unknown and projecting the spectrum onto $\mathbf{b}$. In the field of chemometrics, this estimate is known as a prediction of the analyte concentration because it is an estimate of the concentration that the reference method would provide if the unknown sample were submitted for analysis.

After finding $\mathbf{b}$, unknown samples are evaluated by measuring their spectra and calculating their predicted concentration as

$$\hat{y}_i = \mathbf{b} \cdot \mathbf{x_i}. \tag{1}$$

Equation (1) describes a least-squares regression model with an intercept of zero, which is obtained if the spectra are pretreated by mean centering (subtraction of the average calibration spectrum), or alternatively if the concentrations are taken to include the offset from nonpretreated spectral data.

MOC is applied in this prediction step. The MOC model, however, is produced by designing an optical interference filter whose spectrum encodes a regression vector.[5] We have referred to these specialized interference filters as multivariate optical elements (MOEs).

In previous work, the MOE was designed for operation at a 45° angle of incidence so that both transmission and reflection from the MOE are readily measured. The unscaled regression vector can then be described in terms of $\mathbf{T} - \mathbf{R}$, where $\mathbf{T}$ and $\mathbf{R}$ are the spectral transmission and reflection functions of the MOE.[2] If we include a gain or scaling factor, G, and

The authors are with the Department of Chemistry and Biochemistry, University of South Carolina, Columbia, South Carolina 29208. The corresponding author's e-mail address is myrick@sc.edu.

Received 25 April 2006; revised 5 September 2006; accepted 27 October 2006; posted 31 October 2006 (Doc. ID 70010); published 12 February 2007.

0003-6935/07/071066-15$15.00/0

an offset, O, to increase the design space, the MOC calculation corresponding to Eq. (1) is given by

$$\begin{aligned}\hat{y}_i &= G(\mathbf{T}-\mathbf{R})\cdot\mathbf{x_i}+O\\ &= G(\mathbf{T}\cdot\mathbf{x_i}-\mathbf{R}\cdot\mathbf{x_i})+O\\ &= G(D_{T,i}-D_{R,i})+O. \end{aligned} \quad (2)$$

In the last line of Eq. (2) we have substituted the intensity measurements of two detectors, one each for the transmitted (D_T) and reflected (D_R) portion of the spectrum for sample i. In the MOC measurement, the product of the MOE regression vector with the spectrum of the unknown analyte is created by placing the MOE in the beam, which also passes through the sample. Summation is obtained by allowing all wavelengths to fall on a detector simultaneously. G is required to scale the ($\mathbf{T}-\mathbf{R}$) vector because it can vary only in the range ± 1 at any wavelength, and O is included as a variable in the design of the MOE to increase the probability of finding good MOE designs.

The advantage of MOC over traditional chemometric prediction is that a simple, application-specific tool can be created from calibration spectra that should have improved performance and dependability compared with conventional instruments. For example, all other types of instruments require the acquisition of a large number of individual data points (one for each wavelength or one for each interferometer retardation) from which to make a prediction of an analyte, while a MOC system requires only two measurements which may be acquired simultaneously. As shown previously, 45° MOC devices have the potential to achieve this increase in speed without surrendering either precision or model accuracy.[6]

A. Imaging

In our laboratories we have been adapting MOC to imaging applications. Imaging presents the problem that different image points are formed from light rays that transit the optical element at different angles. The optical elements designed for imaging must be designed to function at many angles of incidence simultaneously. To distinguish such elements from the simpler and more readily designed MOEs, we term them imaging multivariate optical elements (IMOEs).

Imaging applications also prompt two other significant changes to the implementation of MOC as previously discussed. First, an interference filter in the 45° geometry is subject to a large angular dependence, compounded by the fact that rays at equal angles about the central ray transit the filter at distinctly different angles. The use of an IMOE at normal incidence reduces the angular dependence of the optical element spectrum and reduces the angular spread of the incident light by one half. Second, scene illumination is rarely uniform. To compensate for the lack of uniform illumination, the normalization of the IMOE image to an image with no IMOE (the 0 image) is the preferred measurement approach.

We have previously reported an algorithm that helps minimize the effects of the angular dependence of the IMOE reflection and transmission spectra on the angle of incidence.[7] The algorithm treats the angular dependence of the IMOE spectra as just another interferent and seeks to design IMOEs whose spectra shift with angle of incidence without losing orthogonality to other interferences. This can be successful only in approximation because of the nonlinearity of the phenomenon, and sensitivity is always lost whenever a new interference is added. In addition, the effective IMOE spectrum varies across an image, perhaps causing the optimum values of G and O in Eq. (2) to vary across the image. For the most exacting calibrations, therefore, it would be necessary to perform a secondary calibration of the completed instrument to determine a complete set of pixel-specific gain and offset values. For both of these reasons, it is advantageous to minimize the angular dependence of the IMOE spectra.

A quick inspection readily justifies the use of normal-incidence IMOEs compared to those at 45° (Fig. 1). By normal incidence, we mean that the central rays that form an image—those that would be focused to the center of the image field—transit the IMOE perpendicular to the film planes. The first advantage this provides is that rays at equal angles about the central angle have the same angle of incidence. By comparison, the example provided in Ref. 7 posits an incoming cone of light with a half-angle of 3°, but which gives rise to a 6° range in the angle of incidence of a 45° IMOE (42°–48°). The second advantage of the normal-incidence configuration is a reduction of spectral effects of the angular spread that remains. In addition, the s and p components of the transmission spectrum of a MOE overlap perfectly at normal incidence, but become progressively more offset from one another when the angle of inci-

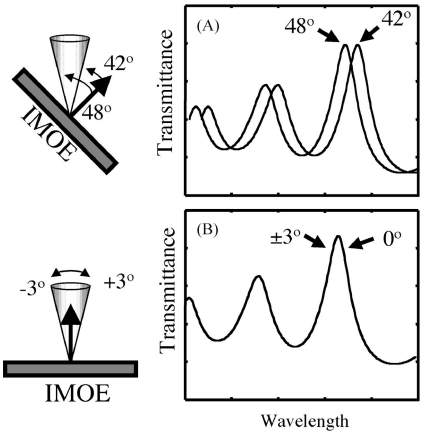

Fig. 1. Comparison of 45° and normal incidence configurations. (A) Left, at an average of 45° incidence, a 6° cone of light strikes an IMOE at angles ranging between 42° and 48° incidence. Right, spectral shift expected for the range of incident angles is relatively large. (B) Left, when the average angle of incidence is normal to the IMOE surface, the same cone of light gives angles ranging from 0° to 3° off normal. Right, reduced angular spread and reduced sensitivity to angular variations causes the spectral shift to be much reduced. A factor of 45 difference between (A) and (B) is illustrated.

dence increases. This requires thicker stacks of films to obtain the same spectral resolution, and means there are two distinct angular nonlinearities added to each IMOE spectrum.

The angular dependence of a peak position in the transmission of an interference filter can be expressed approximately as[8]

$$\lambda(\theta) \approx \lambda_0 \left[1 - \left(\frac{n_0}{n_{\text{eff}}} \right)^2 \sin^2 \theta \right]^{1/2}, \qquad (3)$$

where θ is the angle of incidence (0 at normal incidence), $\lambda(\theta)$ is the peak wavelength as a function of angle θ, λ_0 is the peak wavelength at normal incidence, n_0 is the index of the external medium, and n_{eff} is the effective index of the film stack. A quick example using Eq. (3) will serve to illustrate the points made above.

For a typical interference filter composed of silica and niobia layers, the effective refractive index is approximately 1.9. If the central angle of an IMOE is 45°, then according to Eq. (3), a 6° angular spread (from 42° to 48°) would shift the wavelength of a peak that is nominally at 850 nm by approximately 14 nm. If the central angle were 0°, the same angular spread would cause a shift of only 0.3 nm, a 45-fold decrease in variability.

The decreased angular sensitivity can also be used to expand the field of view (FOV) of an imaging MOC system. Using the same example, if a system can be designed to bear a 14 nm shift in the IMOE spectrum, then the 45° configuration provides only a 6° FOV. At normal incidence, the same tolerance would yield a FOV of 40°. This translates into a dramatically greater FOV for a system operating at normal incidence and with the same degree of correction applied by our previous imaging design algorithms.

The second change to the system design and layout prompted by imaging applications is in the area of normalization. There are many types of normalization used in spectroscopic applications, but the simplest to implement in a MOC setting is the so-called 1-norm, dividing the spectral intensity at each wavelength by the integrated spectral intensity over all wavelengths. This is a useful tool whenever the optical spectra are dominated by overall changes in intensity that are not strongly related to factors of interest. Imaging by reflected or backscattered light depends strongly on the illumination of the scene and its uniformity, so normalization can be used to remove this factor from the calibration.

In MOC in a 45° geometry, the sum of reflectance and transmittance of a typical optical element is very nearly the integrated intensity. A normal-incidence geometry, however, makes it difficult to measure both transmittance and reflectance at the same time. A simple solution is to place the IMOE on a filter wheel and record two different images, one with the IMOE and one without it. The image recorded without the IMOE (a measurement we will refer to as the 0 measurement below) has an intensity given by the integrated reflectance spectrum of the scene and can be used for normalization. Because of possible intensity fluctuations in the time between these nonsimultaneous measurements, a more complicated normalization scheme may be applied in which a reference area within each image is used as an internal standard prior to normalization.

A modified version of Eq. (2) can be written to account for normalization in the normal-incidence configuration. First, since transmission and reflection sum to unity in the case of absorption-free IMOEs, we can write the IMOE spectral function in terms of transmission alone using the equality $\mathbf{T} - \mathbf{R} = 2\mathbf{T} - \mathbf{1}$. If the IMOE films have absorbance, the same substitution can be used, but the equality no longer holds and IMOE design must be based directly on the $2\mathbf{T} - \mathbf{1}$ form.

Second, normalization by the 1-norm means dividing the scalar product by the summed intensity of the sample spectrum over all wavelengths without filtering. This denominator is the same as the scalar product of the spectrum with a vector of ones. Making both changes to Eq. (2) yields, after simplification,

$$\hat{y}_i = 2G \frac{\mathbf{T} \cdot \mathbf{x_i}}{\mathbf{1} \cdot \mathbf{x_i}} + O' \quad \text{where } O' = (O - G). \qquad (4)$$

In this paper, we describe how the noise characteristics of this new configuration compare to the 45° design, how the sign with which the IMOE vector is implemented matters, and what this tells us about how to choose the optimal IMOE design.

One consequence of the normal-incidence configuration is that the sign with which the IMOE regression vector is encoded generally affects the precision of measurement, unlike the 45° geometry. IMOE spectral functions with opposing signs have identical model standard errors of calibration and prediction (SECs and SEPs), and have gain (G) values with identical magnitudes so that every significant aspect of their model behavior is identical. However, they may allow different total amounts of light from the sample to pass through the IMOE, and this affects photon-counting noise, and thus it also affects measurement precision.

This last theoretical conclusion about system precision is confirmed by experimental measurements of a simple model one-component chemical system. A single-component system is valid for assessing precision in measurement and makes facile the finding of good models that can be readily fabricated.

While it is extremely difficult to actually design and fabricate IMOEs with exactly opposite spectral functions, we can set up an optical system in which the reflection of the IMOE is used to mimic the transmission of an IMOE with opposite spectral sign. In this case, the effective spectral function can be written as $2\mathbf{R} - \mathbf{1}$. Since $\mathbf{R}$ and $\mathbf{T}$ sum to unity at all wavelengths in IMOEs with no absorbance, this function is equivalent to $\mathbf{1} - 2\mathbf{T}$, the opposite of the spectral function in transmittance mode.

Following the theory, in Section 2, Section 3 describes how test samples were prepared and evaluated and how the optical system for using a single IMOE in both reflection and transmission mode was set up.

2. Theory

Measurement errors in MOC have two sources. The first is attributable to errors in the model expressed in the optical element. If an infinite number of measurements of the same sample were made so that random errors averaged out, model errors would be the source of all the remaining measurement inaccuracies. In the language of this paper, model errors control the accuracy of the measurements. The second source of error is the random nature of optical measurements. If an identical sample is measured several times, the distribution of the measured analytical value is the result of variability in the measured signals. In the language of this paper, the precision is determined by these random fluctuations. Precision is independent of model errors, but may be influenced by the model itself. This paper, like Ref. 6, deals primarily with how precision is controlled by the nature of the measurement configuration and the characteristics of the model expressed in the IMOE.

Normalized imaging can be performed by using several different canonical experimental configurations, some of which are shown in Fig. 2. The first is closely related to the MOE configuration described in Ref. 6 and is illustrated in Ref. 2, in which the IMOE is used in a 45° configuration, and both reflection and transmission are recorded simultaneously. This configuration has the disadvantages of constraining the design of the IMOE and enhancing model errors, but otherwise is most directly related to the calculations of Ref. 6. The second two configurations use the IMOE in normal incidence, constraining the design of the IMOE the least and resulting in the lowest model errors but generally degrading the measurement precision to a greater or lesser degree.

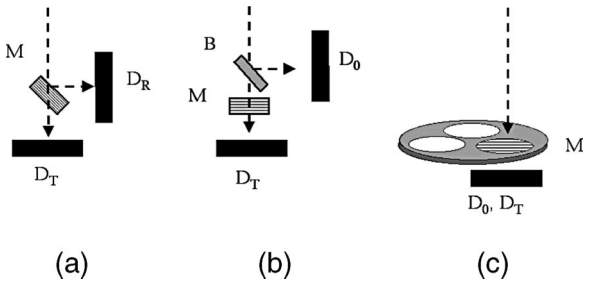

Fig. 2. Configurations for imaging MOC analyzed in this paper. *M* represents the MOE or IMOE position; B represents a beam splitter; D represents a detector for transmission (subscript *T*), reflection (subscript *R*) or open (subscript 0) measurements. (a) Configuration used for all 45° degree incidence calculations. (b) Generic configuration used for normal incidence calculations except for those using a filter wheel. (c) Configuration used for filter-wheel calculations.

The following subsections develop expressions for the standard deviation of measurement errors using the 45° configuration and three distinct implementations of the normal-incidence configuration for comparison. The mathematical notation and treatment follow those found in Ref. 6. We take as given that IMOEs can be designed with comparable models under all the conditions described below, even if the FOV may need to be restricted for 45° applications. Our purpose is to describe how normalized imaging MOC precision varies with the measurement configuration, from the 45° incidence MOE-like geometry to various normal-incidence IMOE configurations. From this discussion, we hope to compare how the model and sign of the model expressed in the IMOE modulate the measurement precision, and to what extent. We begin this analysis by briefly recapping the results of the nonnormalized measurement in the 45° MOE configuration.

A. Nonnormalized Imaging Multivariate Optical Computing at 45° Incidence

Precision using the 45° IMOE configuration [Fig. 2(A)] without normalization for MOC is described exactly as in Ref. 6. In the nonnormalized configuration, the calibration equation, Eq. (1), can be written as

$$\tilde{\mathbf{b}} = \frac{\mathbf{b}}{\|\mathbf{b}\bar{\xi}\|},$$

$$\hat{y} = \bar{g} \sum_{j=1}^{J} \tilde{b}_j \xi_j, \quad \text{where } \bar{g} = T\bar{X}'\|\mathbf{b}\bar{\xi}\|,$$

$$\|\mathbf{b}\bar{\xi}\| \equiv \sqrt{\sum_J b_j^2 \bar{\xi}_j^2}. \tag{5}$$

In this equation, $\bar{g}$ is a gain value in calibration units, T is the total experimental measurement time, $\bar{X}'$ is the total possible photon detection rate, ξ_j is the spectral intensity of a sample at wavelength j normalized to the integrated intensity of the average calibration spectrum, and $\mathbf{b}$ is a loading or regression vector. In the equation, an overbar indicates the quantity is obtained from the average calibration spectrum, and the tilde represents a particular type of normalization applied to the loading vector (for details see Ref. 6).

Reference 6 evaluates the standard error of the MOE chemometric predictions by substituting a function of the reflection and transmission of a MOE in place of the regression vector. The resulting equation is then manipulated until the predictions are placed in terms of detector responses. From this point, we propagate the error in detector responses into the error of predictions and finally assume the noise in a detector response follows Poisson statistics of single-photon counting. The final form of the standard error in Ref. 6 is found by simplifying the resulting error expression following substitution for the detector responses in terms of the properties of the MOE itself. The result can be written as Eq. (6) where $\mathbf{\Delta}$ is the

vector of differences in transmission and reflection ($\mathbf{T} - \mathbf{R}$) of the IMOE element at each wavelength, and $\|\Delta\bar{\xi}\|$ is the 2-norm of the product of the vectors $\mathbf{\Delta}$ and $\bar{\boldsymbol{\xi}}$.

$$\sigma_{\mathrm{MOE}} = \frac{|\bar{g}|}{\left(T\bar{X}'\right)^{1/2}\|\Delta\bar{\xi}\|}. \tag{6}$$

In Eqs. (5) and (6), a discrete wavelength formulation is used to describe what is, in MOC, a continuous function of wavelength. This is done to maintain continuity with conventional spectroscopy and, under the condition that the discrete wavelengths are taken, at a resolution to assure they form a close approximation to the continuous function. We will use this discrete formulation throughout the remainder of this work.

B. Normalized Imaging Multivariate Optical Computing at 45° Incidence

The general calibration equation for calibration data normalized by the 1-norm is given by

$$\hat{y} = \sum_{j=1}^{J} b_j \left(\frac{x_j}{\sum_{i=1}^{J} x_i} \right) = \sum_{j=1}^{J} b_j \left(\frac{\xi_j}{\sum_{i=1}^{J} \xi_i} \right). \tag{7}$$

Following the development in Ref. 6, we replace x_j by the unitless relative intensity, ξ_j, which is normalized to the average calibration spectrum and replace the regression vector component by its unitless equivalent $\tilde{b}_j$ to obtain

$$\hat{y} = \bar{g}_1 \sum_{j=1}^{J} \tilde{b}_j \left(\frac{\xi_j}{\sum_{i=1}^{J} \xi_i} \right), \quad \text{such that } \bar{g}_1 = \|\mathbf{b}\bar{\xi}\|. \tag{8}$$

Note that the gain in Eq. (8) has a subscript 1 to indicate it is for a calibration set that is normalized to the 1-norm. We can make another observation about the nature of this gain value. If we evaluate Eq. (7) for the average calibration spectrum, we obtain

$$\bar{y} = \sum_{j=1}^{J} b_j \left(\frac{\bar{\xi}_j}{\sum_{i=1}^{J} \bar{\xi}_i} \right) = \sum_{j=1}^{J} b_j \bar{\xi}_j = \langle b \rangle, \tag{9}$$

where $\bar{y}$ is the model value associated with the average calibration spectrum and $\langle b \rangle$ is the average component value of the loading vector, weighted according to the average calibration spectrum. It is convenient, then, to think of the regression vector as composed of deviations from the mean weighted value, δb, at each wavelength channel, yielding a modified calibration expression:

$$\hat{y} - \bar{y} = \sum_{j} \delta b_j \left(\frac{\xi_j}{\sum_{j} \xi_i} \right). \tag{10}$$

The left-hand side of this expression is the model value for the regression centered to the value of the mean calibration spectrum, and it is therefore apparent that only the deviations from the mean loading value affect the prediction, a fact that is not true for nonnormalized measurements. In conventional calibration, we would not concern ourselves overmuch about this point because the loading vector in a digital calculation can have any required value. However, in MOC the expression of the loading vector is restricted to values achievable with an interference filter. While we can add constraints in the design process to restrict our designs for IMOEs to have mean values of zero, this constraint might eliminate many useful designs and make practical designs difficult to achieve. The drawback of not using this constraint is that, if the weighted average of the IMOE vector differs greatly from zero, the deviations from the average must therefore vary over a restricted range, causing the effective gain of the system to increase. Because measurement noise is directly proportional to gain, we can expect the magnitude of the weighted average of the IMOE spectrum to correlate directly with increased noise. The minimum value of gain, $\bar{g}_1$, is found when the weighted mean of the loading vector is exactly zero. This allows us to write.

$$\bar{g}_{1,\min} = \|\delta\mathbf{b}\bar{\xi}\|,$$

$$\frac{\bar{g}_1}{\bar{g}_{1,\min}} = \frac{\|\mathbf{b}\bar{\xi}\|}{\|\delta\mathbf{b}\bar{\xi}\|} = \frac{\|\tilde{\mathbf{b}}\bar{\xi}\|}{\|\delta\tilde{\mathbf{b}}\bar{\xi}\|}, \quad \text{where } \tilde{b} = \frac{\langle b \rangle + \delta b}{\|\mathbf{b}\bar{\xi}\|} \equiv \langle \tilde{b} \rangle + \delta\tilde{b}. \tag{11}$$

The vector expressed in the IMOE can be described by the quantity derived in Ref. 6:

$$\Delta_j \equiv t_j - r_j,$$

$$\tilde{\Delta}_j \equiv \frac{\Delta_j}{\|\Delta\bar{\xi}\|} = \tilde{b}_j, \tag{12}$$

where t_j and r_j represent the components of transmission and reflection of the IMOE at wavelength j, respectively. It follows then that

$$\bar{g}_1 = \frac{\|\Delta\bar{\xi}\|}{\|\delta\Delta\bar{\xi}\|}\,\bar{g}_{1,\min} = \frac{\|\Delta\bar{\xi}\|}{\|(\Delta - \langle\Delta\rangle)\bar{\xi}\|}\,\bar{g}_{1,\min}, \tag{13}$$

where $\langle\Delta\rangle$ is a scalar value that is the average of the IMOE function weighted by the mean calibration spectrum intensities. We refer to $\langle\Delta\rangle$ as the weighted vector mean in the following treatment.

Since the IMOE filter function Δ has values that cannot exceed an absolute value of unity at each wavelength, if the weighted vector mean of the IMOE

becomes significant, the apparent gain can become large. Continuing, we follow the procedure outlined in Ref. 6 to write an expression for the detector measurements made using normalized imaging and substitute them into the calibration equation. Suitable expressions are

$$D_T = T\bar{X}' \sum_J t_j \xi_j, \quad D_R = T\bar{X}' \sum_J r_j \xi_j, \tag{14}$$

where D_T represents the measurement of intensity when the light passes through the IMOE, and D_R represents the measurement of light reflected from the MOE. We assume that both detectors (which may be two parts of the same imaging detector) are staring at the sample during the entire measurement time. The calibration equation in terms of detector measurements can be written as

$$\hat{y} = \frac{\bar{g}_{1,\min}}{\|(\Delta - \langle\Delta\rangle)\bar{\xi}\|}\left(\frac{D_T - D_R}{D_T + D_R}\right). \tag{15}$$

It is useful to note that when IMOEs are designed, a gain value such as illustrated in Eq. (4) is always generated to relate the detector measurements to the calibration values. If we denote the value of gain returned by the design optimization function as G_1 for this type of measurement system, Eq. (15) shows that

$$G_1 = \frac{\bar{g}_{1,\min}}{\|(\Delta - \langle\Delta\rangle)\bar{\xi}\|}. \tag{16}$$

This provides a tool for evaluating designs of MOEs and IMOEs because it is possible to perform conventional chemometric analyses to estimate a value for $\bar{g}_{1,\min}$. If we then assume the value of the denominator is equal to the length of the normalized mean calibration spectrum, we obtain a lower-bound value for the design gain that is achievable. If we observe values returned significantly below this lower bound, it is safe to assume the model in the MOE or IMOE is not predictive, a fact that should be evident from the predicted calibration figures of merit.

From Eq. (15) using the definitions given above for the detector signals and making the assumption of photon-limited detection noise, we can obtain for the high-signal-limit measurement standard deviation:

$$\begin{aligned}\sigma_{N,45} &= \sqrt{2}\left(\frac{|\bar{g}_{1,\min}|}{\left(T\bar{X}'\right)^{1/2}\|(\Delta - \langle\Delta\rangle)\bar{\xi}\|}\right)\sqrt{1 - \left(\sum_J \Delta_j \bar{\xi}_j\right)^2}, \\ &= \sqrt{2}\left(\frac{|\bar{g}_{1,\min}|}{\left(T\bar{X}'\right)^{1/2}\|(\Delta - \langle\Delta\rangle)\bar{\xi}\|}\right)\sqrt{1 - \langle\Delta\rangle^2}. \end{aligned} \tag{17}$$

A factor of the square root of 2 appears in the numerator because errors in the transmission and reflection that give rise to an error in the difference of the two are amplified by normalization. The other square root in Eq. (17) varies between unity when the vector expressed in the IMOE is orthogonal to the average calibration spectrum and a minimum of zero when the weighted vector mean approaches either extreme (−1 or 1) possible for an interference filter. The 2-norm that appears in the denominator also approaches zero in the latter case, but more rapidly than the root in the numerator, causing the standard deviation to blow up under all conditions where the filter spectrum does not average near zero. As a practical matter, the denominator will approach zero whenever the IMOE spectrum does not oscillate significantly. The physical significance of this is that in a normalizing system the signal and reference values cannot be totally correlated with one another for a calibration to succeed.

The condition of orthogonality between the IMOE vector and the average spectrum is also the condition in which the weighted vector mean is zero. This is also the condition in which the transmission and reflection intensities of the average calibration spectrum are equal to one another when divided at the IMOE. In addition, the result for normalized calibrations has the same general character as for nonnormalized calibrations, with precision improving (σ decreasing) as the length (contrast) of the IMOE spectral vector away from its mean increases.

We note that Eq. (17) shows that the sign of the vector embodied in the IMOE does not affect precision in the 45° geometry. If the function changes sign, the value of $\langle\Delta\rangle$ also changes sign. The 2-norm in the denominator involves squaring all the elements, and so the sign change is lost. Likewise, the sign of the mean is lost upon squaring in the numerator. This is consistent with expectation since an optical element with the opposite sign would switch only the intensities measured at the two detectors.

C. Normalized Imaging Multivariate Optical Computing at Normal Incidence

One configuration that can be used for normal incidence measurements uses a neutral beam splitter in the optical path, with one beam directed through the IMOE to a detector and the other directed to a detector without encountering the IMOE [Figure 2(B)]. This configuration preserves simultaneity of measurement, i.e., sample motion and illumination variations are equal for both IMOE measurements.

In terms of measurement precision, this configuration differs in how the measurements relate to the loading vector. The two measurements are transmission and a sampling of the total intensity, which we subscript with 0 below. A satisfactory definition for the two measurements is

$$D_T = \frac{T\bar{X}'}{2} \sum_J t_j \xi_j, \quad D_0 = \frac{T\bar{X}'}{2} \sum_J \xi_j. \tag{18}$$

The factor of 2 in the expressions for detector measurements originates from the fact that each detector can only sample half of the incoming beam at most. We assume both detectors are, however, staring at

the sample simultaneously through the entire measurement period.

We can rearrange the calibration equation into the following form:

$$\hat{y} = \frac{\bar{g}_{1,\min}}{\|(\Delta - \langle\Delta\rangle)\bar{\xi}\|}\left(\frac{2D_T}{D_0} - 1\right). \tag{19}$$

The design of IMOEs for measurements in this configuration returns gain values, G_1, that are identical to Eq. (16) because the definition of G used in the design algorithm excludes the factor of 2.

After some algebraic manipulation from Eq. (19), we can show that the expected standard deviation of measurement is

$$\sigma_{N,0} = \sqrt{6}\left(\frac{|\bar{g}_{1,\min}|}{\left(T\bar{X}'\right)^{1/2}\|(\Delta - \langle\Delta\rangle)\bar{\xi}\|}\right)\sqrt{1 + \frac{4}{3}\langle\Delta\rangle + \frac{1}{3}\langle\Delta\rangle^2}. \tag{20}$$

Comparing Eq. (20) with Eq. (17) the standard deviation of prediction in this normal-incidence configuration is, if we assume a design with negligible $\langle\Delta\rangle$, larger by a factor of $\sqrt{3}$ compared to the result for the 45° geometry. Part of this increase comes from the fact that only half of the possible measurement difference is being measured in this geometry. However, the errors that are made in each of these measurements do not produce correlating errors in normalization, and so we recover a small amount of the error made in the 45° geometry.

Note that the sign of the vector represented in the IMOE can affect precision in this geometry if $\langle\Delta\rangle$ is nonzero. If this occurs, the effective gain increases, which is always detrimental to measurement precision. However, a positive weighted vector mean further increases the effects of measurement error, while a negative mean can offset this effect somewhat.

If we are free to select a neutral beam splitter with a splitting fraction other than 0.5, we may intuit that the best precision would be obtained when the IMOE and 0 measurements have equal measured intensities, but this is not generally the case. The definition we can apply to the detector measurements for varying split fractions is

$$D_T = T\bar{X}'(1-f)\sum_j t_j\xi_j, \quad D_0 = T\bar{X}'f\sum_j \xi_j, \tag{21}$$

where f is the beam-split fraction. The calibration equation must compensate for these beam-split fractions:

$$\hat{y} = \frac{\bar{g}_{1,\min}}{\|(\Delta - \langle\Delta\rangle)\bar{\xi}\|}\left(\frac{f}{1-f}\right)\left(\frac{2D_T}{D_0} - 1\right), \tag{22}$$

and we can then show the general form of Eq. (20) to be

$$\sigma_{N,0} = \left(\frac{1+f}{f(1-f)}\right)^{1/2}\left(\frac{|\bar{g}_{1,\min}|}{\left(T\bar{X}'\right)^{1/2}\|(\Delta - \langle\Delta\rangle)\bar{\xi}\|}\right) \times \sqrt{1 + \frac{2}{1+f}\langle\Delta\rangle + \frac{1-f}{1+f}\langle\Delta\rangle^2}. \tag{23}$$

From this point, it is straightforward to show that the optimum beam-split fraction is

$$f = \frac{1 + \langle\Delta\rangle - \sqrt{2(1+\langle\Delta\rangle)}}{\langle\Delta\rangle - 1}. \tag{24}$$

For a weighted vector mean of 0, the optimum split fraction is, as expected, less than unity -0.414. However, the value is not as low as $\frac{1}{3}$ (the intuitive result) because of the difference in the gain factors for the two detectors. The error in the ratio does reach a minimum at that point, but the gain also begins to decrease and partly offsets this apparent improvement. A plot of the optimum split fraction as a function of the mean vector value is shown in Fig. 3.

However, the benefits to be derived from selecting the optimal beam-split fraction are often rather small. If the weighted vector mean is zero, the constant factor of $\sqrt{6}$ that appears in Eq. (20) becomes $(1 + \sqrt{2})$, an improvement of approximately 1.5%. If the mean vector is greater than zero, the benefit of tailoring the neutral beam splitter is reduced even further. If the mean vector value is less than zero, the benefit increases somewhat. For a weighted vector mean of -0.5, the optimal split fraction is $\frac{1}{3}$, and the benefit in precision rises to approximately 5%. The improvement by choosing an optimal beam splitter is thus generally rather small until the value of the mean vector approaches -1. Such an IMOE would never be selected for production unless physical limitations of material choices make better IMOE designs impossible (e.g., if all materials absorb strongly, leading to low average transmission). In summary, then, the benefits of tailoring the beam-split fraction in a nor-

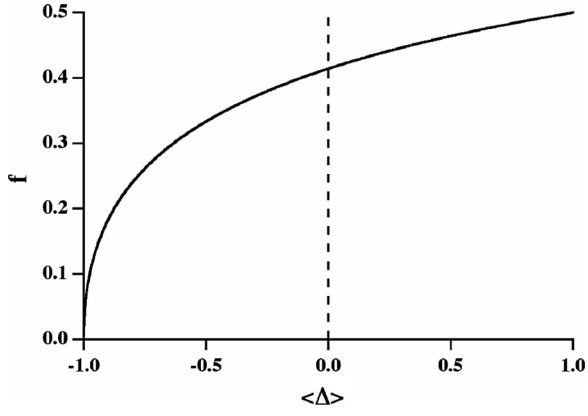

Fig. 3. Optimal beam-split fraction, f, as a function of the weighted vector mean, $\langle\Delta\rangle$, of the IMOE used for imaging in the configuration shown in Fig. 2(c).

malized instrument appear to be negligible under most (hopefully) realistic conditions.

D. Normalized Filter-Wheel Imaging Multivariate Optical Computing

Filter wheels are the simplest implementation of imaging MOC [Fig. 2(C)] because they do not require the design of complicated folding optics to place images on the same detector or selection of matched imaging systems. Suitable expressions for detector measurements in this case are

$$D_T = \frac{T\bar{X}'}{2}\sum_J t_j\xi_j, \quad D_0 = \frac{T\bar{X}'}{2}\sum_J \xi_j. \tag{25}$$

Here the factor of 2 enters by assuming the total experiment time is evenly divided between the IMOE and open-window measurements. Because the forms of the detector signals and the fundamental calibration expressions are the same for this approach as for the preceding case, the results must therefore be the same.

However, when only one of these quantities is measured (as in a filter-wheel implementation of normalized imaging), the sign affects the precision as well. While in general there is no exact way to design interference filters encoding the same vector with opposite signs, the effect can be readily mimicked by using a filter in reflectance rather than in transmittance mode. In such a case, t in the preceding equation would be replaced by r with no other changes, giving a different value to the theoretical precision. The greatest possible value of transmittance is unity at all wavelengths (e.g., for the trivial case of a total band intensity measurement); reflectance has the same value as the IMOE transmission function of the opposite sign: both would be zero in this case. Substituting these values into the preceding equation, we can see that the maximum difference that can be caused by using the same vector with different signs in a filter-wheel IMOE implementation is a factor of $\sqrt{2}$. Filter functions with smaller transmission overlaps with the calibration spectra give the best precision.

E. Normalized Filter-Wheel Imaging Multivariate Optical Computing with a Reference Area

If the instability of the illumination or the sample makes it necessary to utilize a reference area in the same image for each position of the filter wheel, two additional measurements are made in compensation. The design of the MOE or IMOE is performed as if no reference is to be used, but the experimental application of the IMOE uses the reference area as an internal standard and a secondary calibration is then performed to determine experimental values for gains and offsets.

In this case, we consider the maximum rate of photon detection to vary between the transmission and 0 measurements but to have a fixed relationship for pixels within the same image. The reference area is selected to contain a fixed scene element, so that the detector measurements can be described by

$$D_T = \frac{T\bar{X}'_T}{2}\sum_J t_j\xi_j,$$

$$D_{TR} = \frac{T\bar{X}'_{TR}}{2}\sum_J t_j\xi_{j,R},$$

$$D_0 = \frac{T\bar{X}'_0}{2}\sum_J \xi_j,$$

$$D_{0R} = \frac{T\bar{X}'_{0R}}{2}\sum_J \xi_{j,R}, \quad \text{where } \frac{\bar{X}'_T}{\bar{X}'_{TR}} = \frac{\bar{X}'_0}{\bar{X}'_{0R}}. \tag{26}$$

In this case, the experimental ratio that is recorded is

$$\begin{aligned}\frac{D_T/D_{TR}}{D_0/D_{0R}} &= \frac{\bar{X}'_T/\bar{X}'_{TR}}{\bar{X}'_0/\bar{X}'_{0R}}\frac{\sum_J t_j\xi_j/\sum_J t_j\xi_{jR}}{\sum_J \xi_j/\sum_J \xi_{jR}} \\ &= \left(\frac{\sum_J \xi_{jR}}{\sum_J t_j\xi_{jR}}\right)\frac{\sum_J t_j\xi_j}{\sum_J \xi_j} \\ &= \frac{2}{\rho}\frac{\sum_J t_j\xi_j}{\sum_J \xi_j} = \frac{1}{\rho}\left[\frac{\sum_J \Delta_j\xi_j}{\sum_J \xi_j} + 1\right]\end{aligned}$$

$$\therefore \frac{\sum_J \Delta_j\xi_j}{\sum_J \xi_j} = \rho\frac{D_TD_{0R}}{D_0D_{TR}} - 1, \quad \text{where } \rho = 1 + \langle\Delta_R\rangle, \tag{27}$$

where $\langle\Delta_R\rangle$ is the weighted vector mean of the IMOE where the weighting is supplied by the reference. We make the assumption here that the variations in illumination in the scene are relatively small (although large enough to require an internal reference), so that the standard deviation of the measurements attributable to photon counting is not appreciably affected by the variations in illumination. This is exactly the situation we describe in Section 3 that follows, where the variation of illumination was of the order of a percent or less, but was larger than the errors attributable to signal measurement.

The calibration equation can then be written as

$$\begin{aligned}\hat{y}_{N,R} &= \frac{\bar{g}_{1,\min}}{\|(\Delta - \langle\Delta\rangle)\bar{\xi}\|}\frac{\sum_{j=1}^{J}\Delta_j\xi_j}{\sum_{i=1}^{J}\xi_i} \\ &= \frac{\bar{g}_{1,\min}}{\|(\Delta - \langle\Delta\rangle)\bar{\xi}\|}\left(\rho\frac{D_TD_{0R}}{D_0D_{TR}} - 1\right).\end{aligned} \tag{28}$$

As mentioned earlier, the design of the IMOE for this type of system does not involve the use of a reference measurement because each calibration spectrum is individually normalized before convolution with the filter function, and the transmission and 0 measurements are inherently matched. In ap-

plication, however, the 0 measurement is made at a different time and possibly under different conditions. Once a system is built for imaging measurements using this technique, the reference area and subject can be selected randomly, taking serendipitous advantage of the image scene itself, or can be built into the scene on purpose. In either case, a quantitative measurement of the properties of the scene requires secondary calibration based on viewing calibrated samples and fitting the resulting measurements to an equation of the form

$$\hat{y}_{N,R} = \gamma \frac{D_T}{D_{TR}} \frac{D_{0R}}{D_0} + \beta. \tag{29}$$

Note that in Eq. (29) D_{0R}/D_{TR} should be a constant since for all images these reference areas are the same (except for ~1% variations due to fluctuations in illumination between measurements), although the act of measuring them will affect precision since they contribute noise. Comparing Eq. (29) with Eq. (28),

$$\gamma = \rho \left\langle \frac{D_{TR}}{D_{0R}} \right\rangle G_1, \tag{30}$$

where G_1 again is the design gain for the IMOE and $\langle D_{TR}/D_{0R} \rangle$ is the average ratio of the reference area measurements with the IMOE to those in the 0 position. This latter appears in the definition of γ because the IMOE is designed without including a reference area.

A plot of the detector responses as described in Eq. (29) can be used to determine γ. By its definition, ρ is a value that varies around unity, although it can technically range between 0 and 2. The reference area ratio is of the order of the average transmission of the IMOE, although it can also technically assume any value in a range between 0 and 1, depending on the IMOE design and the reference area selected. Consequently, the experimental value of γ is likely to be of the same magnitude as G_1, and of course with the same units.

The precision of measurements made in this way will be characterized in the high-signal, photon-noise-limited condition by a standard deviation of

$$\sigma_{N,R} = \|\gamma\| \sqrt{\frac{2(1 + \langle\Delta\rangle)\left[(1 + \langle\Delta\rangle)(1 + \langle\Delta_R\rangle)\bar{X}'_{TR}\left(\bar{X}'_{TR} + \bar{X}'_T\right) + 2\bar{X}'_{0R}\left(\bar{X}'_T + \langle\Delta\rangle\bar{X}'_T + \bar{X}'_{TR} + \langle\Delta_R\rangle\bar{X}'_{TR}\right)\right]}{T\bar{X}'_T\bar{X}'_{TR}\bar{X}'_{0R}(1 + \langle\Delta_R\rangle)^3}}. \tag{31}$$

To simplify this expression in a way that gives comparative physical insight, we make the following simplifying assumptions. First, we assume that the illumination of the scene, if not uniform, is at least approximately so, in which case the illumination of the reference and sample areas are nearly equal. Second, we assume that the spectrum of the reference is close enough to the average calibration spectrum of the sample that the weighted vector means are the same whether the weighting comes from the sample or the reference. Third, we assume that the change in illumination between the IMOE and 0 measurements is small enough to neglect in the calculation of noise. In this case, the expression (31) simplifies to

$$\begin{aligned}\sigma_{N,R} &= \sqrt{12}\, \frac{\|\gamma\|}{\left(T\bar{X}'\right)^{1/2}} \sqrt{\frac{1 + (1/3)\langle\Delta\rangle}{1 + \langle\Delta\rangle}} \\ &= \sqrt{12}\, \frac{|\bar{g}_{1,\min}|}{\|(\Delta - \langle\Delta\rangle)\bar{\xi}\|\ \left(T\bar{X}'\right)^{1/2}} \sqrt{1 + \frac{4}{3}\langle\Delta\rangle + \frac{1}{3}\langle\Delta\rangle^2}.\end{aligned} \tag{32}$$

If the IMOE can be designed with a weighted vector mean of zero, then this referenced technique represents the least precise of all the methods thus far described, with a standard deviation larger than the nonreferenced approach of by another factor of $\sqrt{2}$. Consequently, the only reason for using internal referencing is to solve the problem of varying illumination intensities.

As seen for the nonreferenced normalization method, the sign of the IMOE vector affects precision, with the positive values of the weighted vector mean causing poorer precision than do the negative values, even though the apparent gain is the same for either measurement. A positive mean is the result of having an average transmission value greater than 0.5, while a negative mean results from average transmissions less than 0.5.

For Section 3 it is useful to note that the relative precision expected for the same vector implemented with two different signs is

$$\frac{\sigma^-_{N,R}}{\sigma^+_{N,R}} = \sqrt{\frac{1 - (4/3)|\langle\Delta\rangle| + (1/3)|\langle\Delta\rangle|^2}{1 + (4/3)|\langle\Delta\rangle| + (1/3)|\langle\Delta\rangle|^2}}, \tag{33}$$

where we have defined $\sigma^-_{N,R}$ as the standard deviation when the weighted vector mean is negative (low average transmission), and $\sigma^+_{N,R}$ is the same when the weighted vector mean is positive (high average transmission).

3. Experimental

Our experimental purpose was to evaluate the performance of IMOE spectral vectors of the same shape and magnitude, but of opposing signs, for comparison to theory. To do this, an optical system was set up that would allow a single IMOE to be tested in both transmission and reflection modes. The goal of the

optical arrangement was to evaluate samples so that the beam paths used in the transmission and reflection modes would be as similar as possible.

The optical system made use of a filter wheel with the IMOE in one position of the wheel and an opening in a second, allowing the IMOE and 0 measurements to be made in sequence in transmission mode. In the reflection mode a silver mirror was used in place of the opening for the 0 measurement. An internal reference sample was used to cancel the effects of drift in the total light flux illuminating all the samples.

The samples were composed of glass slides with polymer films coated on them containing a near-infrared (NIR) dye. The IMOE was designed to predict the peak absorbance of the dye at 860 nm based on normalized imaging, and the reference measurement was a simple diode array transmission study of the samples.

A. Optical Layout

The illumination of samples consisted of a 6 V/6 W lamp (Linos Photonics, Milford, Massachusetts) lighting a paper surface that served as a spectrally neutral diffuse reflector between 650 and 1100 nm (see Fig. 4). Measurements of the paper showed a very slight spectral dependence that was included in the source spectral profile.

Three slides were placed in front of the screen at the time for imaging, of which only the center slide was exchanged for different samples. The right-most glass slide was marked with an arrow for focusing and alignment purposes, and the left-most slide was a fixed reference slide. The central slide was a calibration sample coated with the same type of polymer film containing NIR dye as described in Subsection 3.B. The image shown in Fig. 5 is a typical calibration 0 image of the three slides in reflection mode.

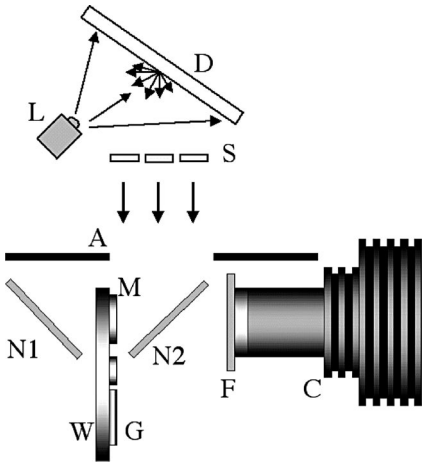

Fig. 4. Schematic of apparatus for measuring prediction precision for an IMOE in reflection and transmission modes. Components are as follows. L, lamp to illuminate samples from behind; D, diffusing screen; S, samples; A, aperture; *N*1, *N*2-Inconel beam splitters; W, filter wheel with IMOE and opening for 0 measurement; M, IMOE; G, silver mirror; F, FGL 715 long-pass Schott glass filter (Thorlabs Inc.); C, camera with lens for imaging. *N*1, *N*2, W, M, G, F, and C were mounted on a translation stage. System is shown in the configuration for IMOE reflection measurement. IMOE transmission measurements were made by translating the camera unit to the right until *N*1 was beneath the aperture.

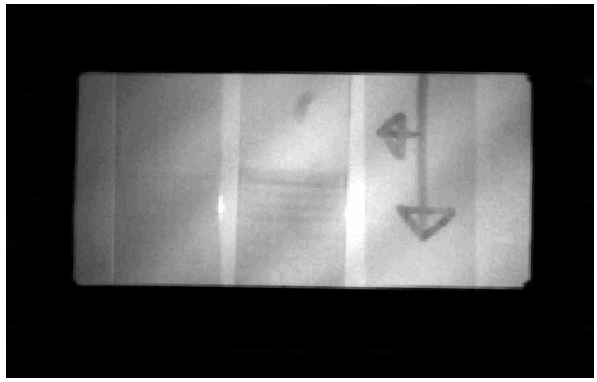

Fig. 5. Typical image of a slide using the MOE in reflection mode. The right slide has an arrow for focus and alignment, the middle slide is the coated slide, and the left slide is a reference slide, which is the same for all images. See text for details on how information in the images was used for calibration purposes.

The camera portion of the system is shown in the lower half of Fig. 4. This optical unit consisted of two Inconel beam splitters, a filter wheel containing the IMOE and an opening for the 0 measurement in transmission mode, plus a plane silver mirror that served as the source for the 0 measurement in reflection mode. The terms T-IMOE and R-IMOE will be used to describe the configurations in which the IMOE is sampled in transmission and reflection, respectively.

The IMOE measurement of the R-IMOE configuration of the optics is illustrated in Fig. 4. The light path illustrated is as follows: (1) Light enters the optical enclosure from the sample through an aperture; (2) light is reflected from the right-most 50/50 neutral Inconel beam splitter at 45° away from the camera lens; (3) light is reflected from the IMOE; (4) light is then transmitted through the same 45° beamsplitter; and (5) light enters the camera lens and filter. All the components just described were mounted together on a translation stage except the aperture (designated A in Fig. 4).

In the 0 (i.e., normalization) measurement of the R-IMOE configuration, the filter wheel is rotated to position a silver mirror in the optical path where the IMOE is shown in Fig. 4. For the 0 measurement using the silver mirror, the exposure times were increased by 2% to compensate for the loss of light during reflection at the silver surface compared to transmission through an opening.

To change the system from R-IMOE mode to T-IMOE mode, the camera assembly is translated to the right in Fig. 4 so that light entering the aperture falls on the left-most 50/50 Inconel beam splitter. The light path from the sample to the camera in the T-IMOE configuration was as follows: (1) Light enters the optical enclosure from the sample; (2) light is reflected from the left-most beam splitter at 45° toward the camera lens; (3) light is transmitted

through the IMOE; (4) light is transmitted through a second beam splitter; and (5) light enters the camera lens and filter. For the 0 measurement, the filter wheel is rotated to position a clear opening in the optical path where the IMOE is shown in Fig. 4. Images taken in T-IMOE and R-IMOE configurations are reversed from one another left to right.

In both R-IMOE and T-IMOE configurations, the filters on the camera and the long-wavelength cutoff of the CCD array itself restrict the wavelength region measured to a band between approximately 700 and 1100 nm. The filter on the camera consisted of a 715 nm Schott glass long-pass filter (FGL 715 Thorlabs Incorporated, Newton, New Jersey). The lens used in the system was an Electrophysics 25 mm $f/1.4$ lens taken from an Indigo Systems Merlin NIR camera. The exposure acquisition times were 0.1 s in all cases except for the 0 measurement using the silver mirror. The silver mirror was measured to have a reflectance of 98% over the wavelength range of interest, so an exposure time of 0.102 s was used to compensate for the intensity loss attributable to reflection at the mirror.

The camera used for this study was an amateur astronomy silicon CCD camera (model ST-6, SBIG Inc., Santa Barbara, California). In Section 2 it was assumed that our camera operates in a photon-noise-limited intensity range and that all pixels have the same performance.

The photon-noise limit was tested as follows. First, the diffuse reflection screen shown in Fig. 5 was replaced with a background that had a large variation of shades of gray ranging between black and white in order to produce a range of pixel responses in each image. A set of 64 images was then acquired under the same illumination conditions at array temperatures of +18 °C and −18 °C.

If photon counting is the source of noise in these measurements, then the standard deviation of the number of photons detected at each pixel should be equal to the square root of the number of photons detected. The standard deviation and the measured intensity in count units should both be proportional to the corresponding values in photon units, where the proportionality constant is the number of photons detected per count. If photon-noise-limited behavior is being observed, a plot of the variance in counts of a given pixel versus the average number of counts for the same pixel, repeated over a range of average measurement conditions, should provide a linear relation with the slope being the reciprocal of the number of photons detected per count. If the pixels all exhibit approximately the same behavior, then a plot based on images with graduated intensities should show the same behavior.

Initial measurements showed that the noise was dominated by lamp intensity drift, indicated by a drift in the total counts summed over all pixels being greater than the minimum demanded by photon counting and showing systematic trends. To compensate for this, all 64 images were normalized to the same total integrated intensity, with the very slight adjustments made considered to have negligible impact on the photon-counting noise at each pixel. For the same reason, our experimental assessment of noise in Subsection 3.B was performed with an internal standard reference slide to compensate for lamp intensity drift and to assure photon-limited behavior.

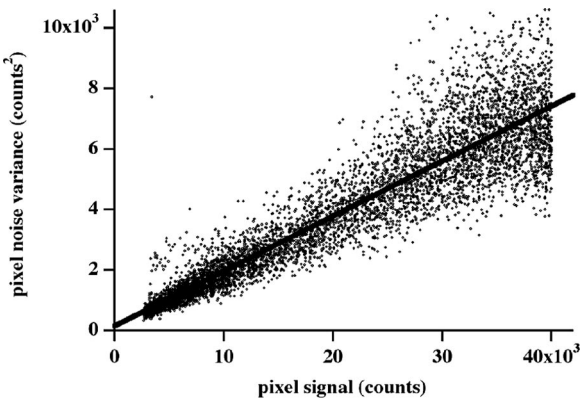

Fig. 6. Photon-noise behavior of detector. Linear relation between the standard deviation of detector counts over several identical measurements versus the square root of detector A/D counts follows the behavior expected for noise limited by photon counting. Each point represents the result for a single pixel measured 64 times on the same scene. The best-fit line shown in solid black yields a slope of 0.1817 ± 0.0009, equivalent to 5.50 ± 0.03 detected photons per count. The intercept is 148 ± 22, equivalent to a noise of 12 counts at zero signal. This plot became nonlinear above 45,000 count units.

The compensated noise plot for the +18 °C case is shown in Fig. 6, which gave a value of 5.50 ± 0.03 photons/count. The −18 °C case gave a value of 6.01 photons/count. The baseline noise was small on the scale of these measurements, so that photon-limited behavior can be assumed in images wherever there is any appreciable image intensity. It was also found during these experiments that above ~45,000 counts [out of a total analog-to-digital (A/D) range of 65,536 counts] the noise profile changed significantly, a fact that can be attributed to the onset of pixel charge saturation. The data from any pixel giving a detector measurement over 40,000 counts were considered unreliable and were not used in this analysis.

B. Calibration Samples

The coated slides were prepared as follows: 0.0696 g of Epolight 4019 (Epolin, Incorporated, Newark, New Jersey) was dissolved in 100 ml of methylene chloride, and 11.0 g of acrylic ester resin (Acryloid B-67, Rohm and Haas, Canada, available from Talas Inc., New York, density = 0.66 g/cm^3) was dissolved in the same mixture to serve as a binding material transparent between 650 and 1100 nm.

A solution of 19.48 mg/l of Epolight 4019 in methylene chloride gave a maximum absorbance of 1.1023 absorbance unit at 862 nm, yielding an approximate specific absorbance of 56.6 l/g/cm. λ_{max} is measured to be 862 nm in methylene chloride and 860 nm in the resin, and we assume the same specific absor-

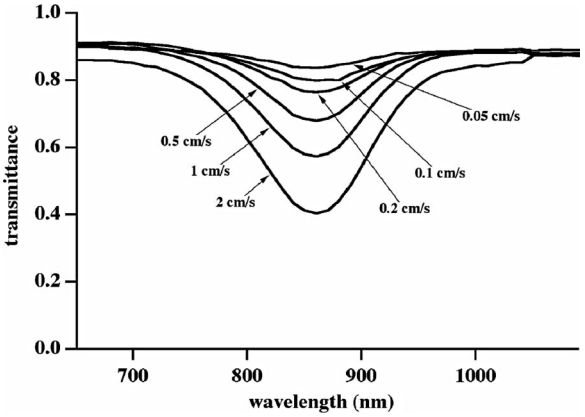

Fig. 7. Transmission spectrum of slides from 650 to 1100 nm. Dip-coat rates (in units of centimeters per second) are 0.05, 0.1, 0.2, 0.5, 1, and 2 in order from the shallowest absorbance to the deepest. From top to bottom, these curves represent the spectra of calibration samples 1–6, respectively.

bance can be attributed to Epolight 4019 in the polymer solution at 860 nm.

Three identical sets of six coated slides were created by dipping the slides into the methylene chloride–polymer–dye mixture and pulling the slides out at the following constant rates: 0.5, 1, 2, 5, 10, 20 s/cm. The transmission spectra of exemplars of each drawing rate are shown in Fig. 7.

The dependence of the film thickness of polymer on the rate of drawing of the dip-coated slides is illustrated in Fig. 8, which shows how the absorption of the center of the slides varies at the maximum absorption at 860 nm with draw rate. The absorbance, and thus the thickness of the polymer film, increased with the increasing draw rate, with a relative precision of approximately 10%. Increasing thickness with draw rate is a well-known phenomenon attributable to viscosity effects in the coating fluid.[9] Based on the specific absorbance of Epolight 4019 (56.6 l/g/cm), the density of the polymer (0.66 g/cm^3), and the mass ratio of the polymer to dye in the stock solutions (158 g polymer/g dye), the total thickness of the polymer films can be estimated as 42.4 μm per absorbance unit at 860 nm. Since the film is coated on both sides of the slide during dip coating, the film thickness on one side is approximately half of the value indicated by the absorbance. This calculation omits any consideration of interference effects or Fresnel reflectances that might differ between the coated and uncoated slide, but by taking the absorbance from the apparent average baseline we can avoid considering these effects to the first order. The results using this calculation are consistent with film thicknesses obtained by measuring interference fringes in the transmission spectrum of undoped films.

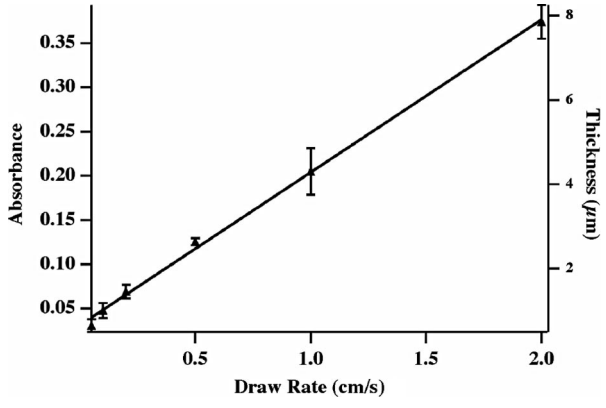

Fig. 8. Absorbance (860 nm) and inferred thickness of coating as a function of the rate of dip coating for slides coated with acrylate polymer from a methylene chloride solution. Standard deviation of absorbance is indicated by error bars. Thickness is the one-sided thickness estimated from bulk density of the polymer, mass fraction of dye, and specific absorptivity of the dye (for details see text).

C. Imaging Multivariate Optical Element Design and Fabrication

IMOE design required radiometric characterization of the spectral response for each element of the system shown in Fig. 4 and then proceeded as previously described.[5,7] The spectral radiance of the lamp, the spectral reflectance of the diffuse reflecting paper, the reflectivity and transmission of the Inconel beam splitters (one reflection and one transmission through the beam splitters was experienced in both T-IMOE and R-IMOE modes), the transmission spectrum of the 715 nm long-pass filter, the spectral efficiency of the lens, and the spectral responsivity of the camera array were all measured separately in our laboratory and multiplied together to obtain an absolute spectral response for the system without the samples. This absolute response was then normalized to unit area to produce a relative system spectral response. Figure 9 shows this relative spectral response multiplied by the transmission spectra of Fig. 7.

The IMOE was fabricated with low-absorbance materials (BK7 optical glass substrates) and films

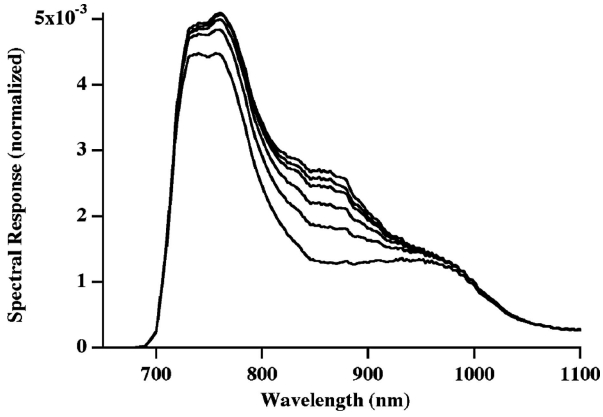

Fig. 9. Calibration data normalized to the area integral of the average calibration spectrum. Curves are the estimated convolved system spectral responses based on calibration transmission spectra and spectroradiometric performance and efficiency of the CCD system and illumination components and optics, excluding the IMOE. Curves, from top to bottom, are calculated for calibration samples 1–6.

(Nb_2O_5 and SiO_2), ensuring that the reflection and transmission of the IMOE at every wavelength in the measured spectrum would sum to unity to a high degree of accuracy. From the IMOE images we then made predictions of the maximum absorbance of the slides as described below.

D. Precision Calculation

The optical layout (Fig. 4) allows light from a sample to interact with the IMOE in either T-IMOE or R-IMOE mode, allowing two measurements of the same IMOE vector but with opposing signs. Because vectors differing only in their signs must have the same SEC, SEP, and even the same magnitude of gain, any difference in their measurement precision originates from factors not considered in Ref. 6.

One sample representing each draw rate/absorbance level was selected as a secondary calibration standard, giving a total of six. A total of 64 images was taken of each sample in the T-IMOE configuration, 32 with the IMOE in place and 32 without the IMOE (i.e., the 0 measurement). This was repeated for the R-IMOE configuration. For each configuration, these measurements permitted the calculation of 32 independent normalized measurements. An average and a standard deviation of the 32 normalized measurements in each configuration were also calculated.

Each normalized measurement was calculated from two independent images as follows. First, a 10 $\times$ 10 pixel section in the middle of the sample slide was chosen, and the pixel values were summed for both the IMOE image and the corresponding 0 image. Each of these results individually were then internally referenced to the summed counts from a 10 $\times$ 10 pixel section in the middle of the reference slide in the same image. This was done to correct for illumination variability between images. The internally referenced result for the IMOE image was then divided by the internally referenced result for the 0 image to produce a single normalized measurement.

The average of 32 internally referenced and normalized measurements for each calibration sample was used for secondary standardization of the imaging MOC system. That is, a least-squares fit of the peak absorbance (the variable being predicted, whose reference value was determined by conventional transmission measurements) to the average normalized measurement was used to determine experimental values for the correlation. This process was performed for both the T-IMOE and R-IMOE configurations because the secondary calibrations of the two configurations were not expected (nor found) to be identical. This is because the quantitative effect of internal referencing to the reference slide differs in the two configurations and is not necessarily known *a priori*.

Once the secondary calibration was performed, it was possible to use the individual internally referenced and normalized measurements from a pair of images to predict the calibrated peak absorbance values. The precision of the system was then determined from the standard deviation of these predictions, which is directly proportional to the standard deviation of the normalized measurements.

4. Results and Discussion

When an IMOE is designed, several characteristics may be used to assess the potential performance of the design in use. First and foremost, model characteristics dominate the selection of designs. A low SEC and SEP are desirable so the prediction of the analyte concentration has optimal accuracy. Following a typical design step, several dozen designs may have been generated that met the criterion of having SECs and/or SEPs that approximate those of conventional chemometric methods for the same measurement.

After winnowing the results by choosing only those designs with small model errors, a second important characteristic is that of gain, G, in Eq. (2). A small gain value is desirable since this indicates an IMOE that is more sensitive to the analyte. Low gains also mean that shifts in the IMOE profile due to deposition anomalies will be less damaging to the predictive behavior of the final IMOE, compared to an IMOE where predictive behavior depends strongly on weak features. In addition, errors in deposition require redesign of the IMOE, and this generally demands increasing the gain to recover model accuracy. In this sense, a low gain corresponds to a higher error budget during fabrication. For the same reason, an IMOE with a small gain is also likely to be more tolerant to drifts in the calibrated system, and has a wider window in which a compensation for this drift could be applied.

Another factor that is important in selecting an IMOE design from the available list of possible designs generated by the design algorithms is the error attributable to the photon-counting noise that is the basis for the preceding calculations. The MOC system collects all light over a region of the spectrum. As a result some regions are measured that do not contain useful information pertaining to the analyte. However, this region will still contribute noise to the overall result. The exact behavior regarding the noise is intrinsically dependent on the IMOE profile and cannot be estimated from values such as the SEC, SEP, or even from the gain alone (although the preceding shows that gain is an important factor).

Figure 10 shows the transmission ($\mathbf{T}$) and reflection ($\mathbf{R}$) profiles for the IMOE, which was designed for this measurement, and the two possible encoded regression vectors taken as $(2\mathbf{T} - \mathbf{1})$ and $(2\mathbf{R} - \mathbf{1})$. To make use of Eq. (33) for estimating the relative precision of these two regression vectors, we must determine their weighted vector means. The weighted vector mean is determined by convolving the system response with the calibration spectra, determining their average, normalizing that average to unit area, and calculating the direct product of the normalized average with the IMOE vector.

Figure 9 shows the simulated calibration set spectra used for these experiments. The average of the curves in Fig. 9 was normalized to unit area and used

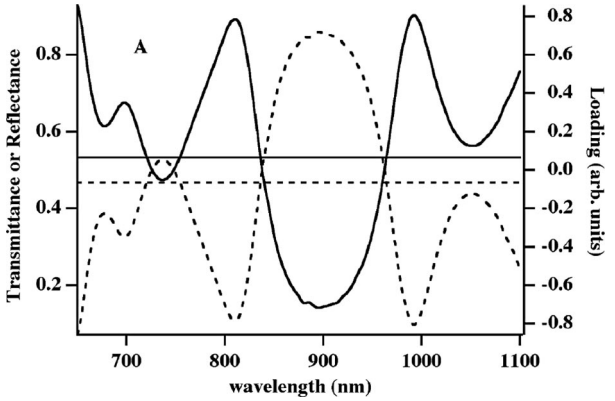

Fig. 10. Fabricated IMOE transmission, reflection, vectors, and averages. Solid curves correspond to transmission properties, while dashed curves correspond to reflection properties. Transmission and reflection are read from the left axis, while the corresponding vectors are read from the right axis. The right axis is obtained as $2T$-1 or $2R$-1 for transmission or reflection modes, respectively. The right-hand label "arbitrary units" indicates that these values are unscaled by the gain of the system. Solid and dashed straight lines refer to the transmission and reflection weighted averages, respectively. The transmission vector is assigned to the (+) terms in Eq. 33 because its weighted vector mean is +0.0660. The reflection vector is of equal magnitude but negative, and it is assigned to the (−) terms.

to determine the average transmittance, $\langle T \rangle = 0.533$, the average reflectance, $\langle R \rangle = 0.467$, and the weighted vector means of the two vectors, +0.0660 (transmission) and −0.0660 (reflection). These values are shown in Fig. 10 as lines of the appropriate type at the level of the averages. As Fig. 10 illustrates, the relationship between the regression vectors and their means to the transmission and reflection spectra and their respective mean values is very straightforward in the case of nonabsorbing IMOE materials.

From the weighted vector means, we expect the standard deviation of prediction to be better when the IMOE is used in reflection mode than in transmission mode by a factor of 0.916.

Secondary calibration of the optical system in Fig. 4 using the six calibration samples whose spectra are shown in Fig. 7 was performed. The internal reference area selected for these measurements was a region inside the region of another fixed sample in the image. As described in the experimental section, a total of 32 internally referenced normalized values corresponding to the term $(D_T/D_{TR})(D_{0R}/D_0)$ in Eq. (29) were measured for each of the six calibration samples. The peak absorbance of each sample at 860 nm (the value the IMOE was designed to predict) was regressed against the averages of these 32 measurements for each sample to determine secondary calibration coefficients corresponding to γ and β in Eq. (29). The resulting values are summarized in Table 1.

Using a secondary calibration based on the averages of the values, it was possible to predict the absorbance for each of the 32 measurements of each calibration sample. This led to a determination of the SEC for each

Table 1. Secondary Calibration Parameters

Mode	γ^a	β^a	$\sigma_{N,R}$
Transmission	9.4342	−9.2601	0.01546
Reflection	−7.722	7.8099	0.01445

[a]Coefficients in Eq. 29.

sample. These values were all similar to one another, the average of which is also provided in the final column of Table 1. The ratio of the standard deviation in reflection mode to that in transmission mode was measured to be 0.935, compared to a theoretical prediction of 0.916. A full repeat of this experiment produced an experimental ratio of 0.944. The experimental result agrees with the theoretical result qualitatively. The reflectance measurement consistently produced better precision than the transmission measurement, and the ratios differ from unity by factors that are within 30% of one another.

Several sources account for the observed quantitative differences between the theoretical and experimental values. The first is related to the adequacy of the secondary calibration because any errors in that calibration result in erroneous slopes that affect precision in direct proportion. Second, we can look at the simplifying assumptions required to obtain Eq. (33). These are: (1) Illumination of the reference and sample areas are nearly equal, (2) the spectrum of the reference is close to the average calibration spectrum, and (3) the change in illumination is small enough to neglect in the calculation of noise. Figure 5 shows that the reference slide (to the left of the sample in the center) is not illuminated as strongly as the sample, so the first assumption is only qualitatively correct. The second assumption is also only qualitatively correct, since none of the six samples presents a spectrum that is identical to the average spectrum, and one of these samples in the central range of concentrations was selected for a reference. The third is probably the most accurate of the simplifying assumptions because the drift in illumination was small (<1% relative drift) on the scale of the total illumination. Because of the inexact nature of the first two of these assumptions, however, the theoretical result is only expected to be a guide.

5. Conclusions

Imaging with multivariate optical computing is improved by using IMOEs designed for normal-incidence use. The benefits of normal incidence include halving the range in angle of incidence compared to the 45° geometry and decreasing the effects of the remaining range of angles on the IMOE spectrum. These improvements can be used to design IMOEs with better predictive performance or to substantially increase the effective FOV of an imaging MOC system.

However, imaging in normal incidence makes it difficult to collect all photons, unlike the 45° geometry. Also, imaging often requires normalization to account for variable illumination of a scene. Precision

is therefore analyzed differently in imaging than in the more well-studied 45° geometry.

An analysis of precision (based on the standard deviation of measurements) for imaging MOC using three important measurement modes has been given. In addition, the validity of the results has been tested using an experimental measurement of precision for a single IMOE to simulate the effects of having the same regression vector encoded in an IMOE with opposite signs.

The results show that, in normal-incidence arrangements, the sign of the encoded vector affects the precision of measurement whenever the average value of the vector, weighted by the loadings of the average calibration spectrum, is nonzero. Experimental results confirm that vectors with negative weighted vector means are preferred compared to those with positive means.

Nonzero weighted vector means also place a lower limit on the achievable IMOE model gain. An IMOE with a vector having significantly nonzero means also usually has a reduced contrast (the difference between the highest and lowest transmittance). The lowest gains possible for an IMOE require that the encoded regression span the greatest possible transmission space of the optical element. In the analytical expressions for precision in this paper, this factor appears as the weighted rms. deviation of the vector from its weighted average.

In addition, a new beam-splitter arrangement (designated B in Fig. 2) is analyzed for applications in imaging MOC, and the optimal beam-splitter fraction is determined. The benefits of the optimal beam-splitter fraction are relatively small, however, suggesting that the best available beam splitter is a suitable choice for most applications.

M. Simcock thanks the University of South Carolina NanoCenter for its support and assistance during the development of this work.

References

1. M. P. Nelson, J. F. Aust, J. A. Dobrowolski, P. G. Verly, and M. L. Myrick, "Multivariate optical computation for predictive spectroscopy," Anal. Chem. **70,** 73–82 (1998).
2. O. Soyemi, D. Eastwood, L. Zhang, H. Li, J. Karunamuni, P. Gemperline, R. A. Synowicki, and M. L. Myrick, "Design and testing of a multivariate optical element: the first demonstration of multivariate optical computing for predictive spectroscopy," Anal. Chem. **73,** 1069–1079 (2001).
3. K. R. Beebe, R. J. Pell, and M. B. Seasholtz, *Chemometrics: A Practical Guide* (Wiley, 1998).
4. H. Martens and T. Naes, *Multivariate Calibration* (Wiley, 1989).
5. O. O. Soyemi, F. G. Haibach, P. J. Gemperline, and M. L. Myrick, "A nonlinear optimization algorithm for multivariate optical element design," Appl. Spectrosc. **56,** 477–487 (2002).
6. F. G. Haibach and M. L. Myrick, "Precision in multivariate optical computing," Appl. Opt. **43,** 2130–2140 (2004).
7. O. O. Soyemi, P. J. Gemperline, and M. L. Myrick, "Design of angle-tolerant multivariate optical elements for chemical imaging," Appl. Opt. **41,** 1936–1941 (2002).
8. V. Saptari and K. Youcef-Tourni, "Design of a mechanical-tunable filter spectrometer for noninvasive glucose measurement," Appl. Opt. **43,** 2680–2688 (2004).
9. A. F. Michels, T. Menegotto, and F. Horowitz, "Interferometric monitoring of dip coating," Appl. Opt. **43,** 820–823 (2004).